Experimental determination of the temperature- and phase-dependent elastic constants of FeRh

D. Ourdani,[1,2] A. Castellano,[3] A. K. Vythelingum,[1] J. A. Arregi,[4] V. Uhlíř,[4,5] B. Perrin,[1] M. Belmeguenai,[2] Y. Roussigné,[2] C. Gourdon,[1] M. J. Verstraete,[3,6] and L. Thevenard[1,*]

[1]*Sorbonne Université, CNRS, Institut des Nanosciences de Paris, 4 place Jussieu, 75252 Paris, France*
[2]*LSPM, Université Paris 13, Sorbonne Paris Cité, 99 avenue Jean-Baptiste Clément, 93430 Villetaneuse, France*
[3]*NanoMat/Q-Mat Université de Liège, and European Theoretical Spectroscopy Facility, B-4000 Liège, Belgium*
[4]*CEITEC BUT, Brno University of Technology, Purkyova 123, 612 00 Brno, Czech Republic*
[5]*Institute of Physical Engineering, Brno University of Technology, Technická 2, 616 69 Brno, Czech Republic*
[6]*ITP, Physics Department, Utrecht University, 3508 TA Utrecht, the Netherlands*

(Received 29 March 2024; revised 30 May 2024; accepted 28 June 2024; published 18 July 2024)

The elastic constants of an epitaxial film of FeRh have been determined experimentally in both ferromagnetic (FM) and antiferromagnetic (AF) phases, using a combination of Brillouin light scattering and picosecond acoustics experiments. The C_{11} constant is noticeably larger in the FM phase than in the AF phase, while C_{12} and C_{44} are both lower, leading to larger Rayleigh wave velocities in the FM phase than in the AF phase. The elastic constants were calculated numerically using first-principles anharmonic modeling and machine-learned interatomic potentials. We find that using a temperature-dependent effective potential is indispensable to correctly reproduce the experimental values to within 80–100%. The accurate knowledge of the temperature- and phase-dependences of the elastic constants of crystalline FeRh are valuable ingredients for the predictive modeling of the acoustic and magnetoacoustic properties of this magnetostrictive material.

DOI: 10.1103/PhysRevB.110.014427

I. INTRODUCTION

FeRh is a fascinating magnetic material discovered in 1938 by Fallot [1]. It is currently being revisited in light of novel magnetic and spintronic applications. Its room-temperature bistable antiferromagnetic (AF) states herald the possibility of robust magnetic encoding [2–5], while its first-order transition to a ferromagnetic (FM) state is responsible for large entropy changes promising solid-state magnetic refrigeration [6,7]. This transition is accompanied by a substantial (∼1%) isostructural volume change [8,9] that is intertwined with the magnetic transition [10,11].

While much attention has been dedicated to the magnetic characteristics of this material, few experimental studies have been devoted to its elastic properties as a function of the magnetic phase and/or temperature. Notably, there is no record of the complete set of elastic constants C_{11}, C_{12}, and C_{44} of crystalline cubic FeRh in the literature. The value of C_{11} is the one that is most readily obtained by measuring the longitudinal acoustic wave velocity and the volume density ρ, with $V_L = \sqrt{\frac{C_{11}}{\rho}}$. Combining this value with a specific heat measurement within a Debye model yields an estimate of the transverse acoustic velocity, and hence C_{44} given that $V_T = \sqrt{\frac{C_{44}}{\rho}}$. This enabled Cooke *et al.* [12] to estimate the values of C_{11} and C_{44} in the AF and FM phases, both obtained at room temperature by imposing slightly different Rh concentrations in two distinct samples. No value has been provided so far for C_{12}, which is more challenging to measure. There are somewhat more data for *polycrystalline* FeRh [13–15], on which it is straightforward to estimate the Young modulus E by measuring bulk acoustic wave velocities. Finally, there is a substantial corpus of theoretical papers reporting density functional theory (DFT) simulations of the phonon band structure of FeRh [16–19], from which the elastic constants in both phases can be estimated. However, to our knowledge, the explicit temperature dependence of C_{ij} has never been determined.

In this work, we measure experimentally the temperature dependence of C_{11}, C_{12}, and C_{44} in both AF and FM phases of a single FeRh crystal by a combination of Brillouin light scattering (BLS) and picosecond acoustic wave interferometry. We follow the strategy developed for other materials by previous authors [20–23], who measured the dispersion relations of phonons, using either inelastic BLS [20,21] or time-of-flight methods [23]. For sufficiently complete data sets including different modes (bulk/surface or Rayleigh/Sezawa), or various crystallographic directions, the elastic constants can be recovered by global fits, e.g., using simplex methods applied to the modeling of the acoustic wave dispersion. Our findings are supported by machine-learning molecular-dynamics simulation fits to *ab initio* data, and they are in agreement with previously published theoretical estimates [16–19], which report a substantially larger C_{11} and lower C_{12}, C_{44} in the FM phase, with respect to the AF one. Moreover, the measured temperature dependence of the elastic constants is very well corroborated by these temperature-dependent simulations.

The first sections of this article are dedicated to a description of the sample, and the BLS and picosecond acoustics

*Contact author: thevenard@insp.jussieu.fr

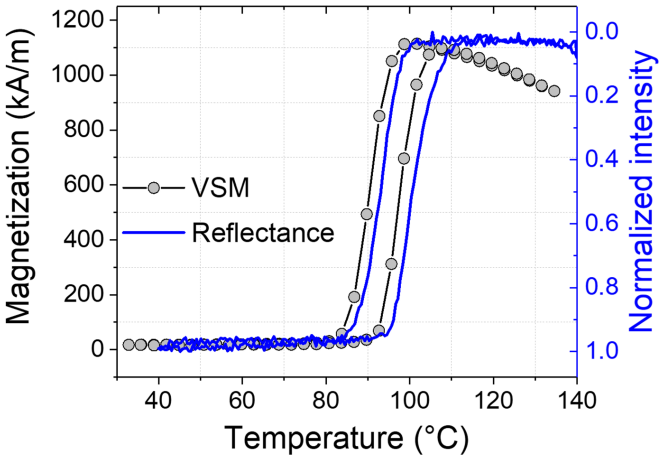

FIG. 1. Characterization of the AF-to-FM phase transition of FeRh using VSM and reflectivity (inverted scale and normalized to its maximal value).

experiments. The following sections describe the analytical modeling of the acoustic dispersion, the resulting deduction of the elastic constants, and a comparison to available theoretical elastic constants from our calculations and the literature.

II. SAMPLE

The epitaxial 195-nm-thick FeRh film under study was grown on a MgO(001) substrate via dc magnetron sputtering from an equiatomic target. The FeRh film was grown at 430 °C after preheating the substrate in high vacuum for 60 min at the same temperature. An Ar pressure of 2.7×10^{-3} mbar and a sputtering power of 50 W led to a deposition rate of 2 nm min^{-1}. The film was then annealed *in situ* in high vacuum at 780 °C for 80 min, and a protective 2-nm-thick Pt capping layer was grown after cooling down the sample below 120 °C. X-ray diffraction characterization shows a high-quality FeRh(001) out-of-plane texture of the sample and the attainment of a homogeneous CsCl-type structure, showing cube-on-cube epitaxy with the FeRh unit cell being 45° in-plane rotated with respect to MgO [9]. Strain in the FeRh film is largely relaxed (with the out-of-plane lattice parameter $c = 2.988$ Å approaching the bulk value) due to the relatively large thickness of the film. Transmission electron microscopy imaging of a cross-sectional lamella allowed a more precise determination of the film thickness, $d = 195 \pm 2$ nm [24].

The AF $\leftrightarrow$ FM transition of the sample is characterized by both vibrating sample magnetometry (VSM, probing the entire volume of the sample) and light reflection microscopy (probing the topmost 10 nm of the film into which the $\lambda_R = 635$ nm light is absorbed). As shown in Fig. 1, the onset of the transition occurs at very similar temperatures with both methods, respectively ≈89 °C/98 °C (warming and cooling branch) from VSM and ≈94 °C/101 °C from light reflection. The slight discrepancy in the transition temperatures obtained by these two methods arises from the difference in the probed area and volume. The transition width is relatively narrow (≈10 °C) and the sample possesses a very low (≈ 16 kA m^{-1}) residual magnetization at room temperature, both confirming the excellent quality of the film.

III. METHODOLOGY

The experimental approach is the following: using Brillouin light scattering, we measure phonon frequencies at fixed temperatures and variable incident wave vectors to extract the temperature-dependent dispersion relationships of the first three acoustic modes (Rayleigh and two Sezawa modes). We then perform temperature-dependent picosecond acoustic wave interferometry to measure the longitudinal velocity and obtain $C_{11}(T)$. Fixing this value, we then adjust $C_{12}(T)$ and $C_{44}(T)$ to reproduce the BLS-measured dispersion curves. To analyze the anharmonic and elastic properties, we perform first-principles calculations for $T = 0$, and then we augment these with a machine-learning interatomic potential (MLIP) to be able to run large molecular-dynamics simulations, and to compute the temperature dependence of phonons and the corresponding elastic constants.

IV. BRILLOUIN LIGHT SCATTERING MEASUREMENTS

A. Description of the experiment

Over the past few decades, BLS has proven to be a powerful technique for characterizing elastic [via surface acoustic waves (SAWs)] and magnetic [via spin waves (SWs)] properties of thin films and multilayer structures. In our BLS experiments, a monochromatic solid-state laser with a wavelength of $\lambda_{\text{BLS}} = 532$ nm and a power of 150 mW is focused onto the sample surface after passing through a set of mirrors and lenses. The backscattered beam from the sample (according to elastic and inelastic processes) is directed to a tandem Fabry-Pérot interferometer at (3 + 3)-pass to determine the frequency shift with respect to the incident beam. The wave-vector (k) is determined by the angle of incidence of the laser with respect to the normal to the sample (θ_{in}) according to the relationship $k = 4\pi \sin\theta_{\text{in}}/\lambda_{\text{BLS}}$. All the measurements carried out in this work were made for a wave-vector parallel to the [100] ([110]) direction of MgO (FeRh).

In Fig. 2(a) we present three spectra obtained for different k values at room temperature (AF phase). Note that in this phase, magnetic modes are expected to be out of the observed frequency range [25]. Three surface acoustic modes can be seen, corresponding to the Rayleigh and the so-called Sezawa guided waves. Lorentzian fits of these spectra are then performed to obtain the positions of the Stokes (S) and anti-Stokes (aS) lines, which correspond to negative and positive frequency shifts respectively, f_{S} and f_{aS}. They were found to be identical in absolute value.

Finally, an *in situ* heating system was integrated into the BLS bench in order to vary the temperature and perform measurements in the uniform AF and FM phases (please refer to Appendix A for technical details). As the temperature was increased to enter the FM phase, a magnetic field of 200 mT was applied to isolate the purely elastic modes.

B. Discussion of $f(T)$ and $f(k)$ curves

Two kinds of spectra were recorded: (i) at a fixed wave vector and variable temperature ($k = 15.18$ μm^{-1}) used to locate the phase transition, and (ii) at a fixed temperature and

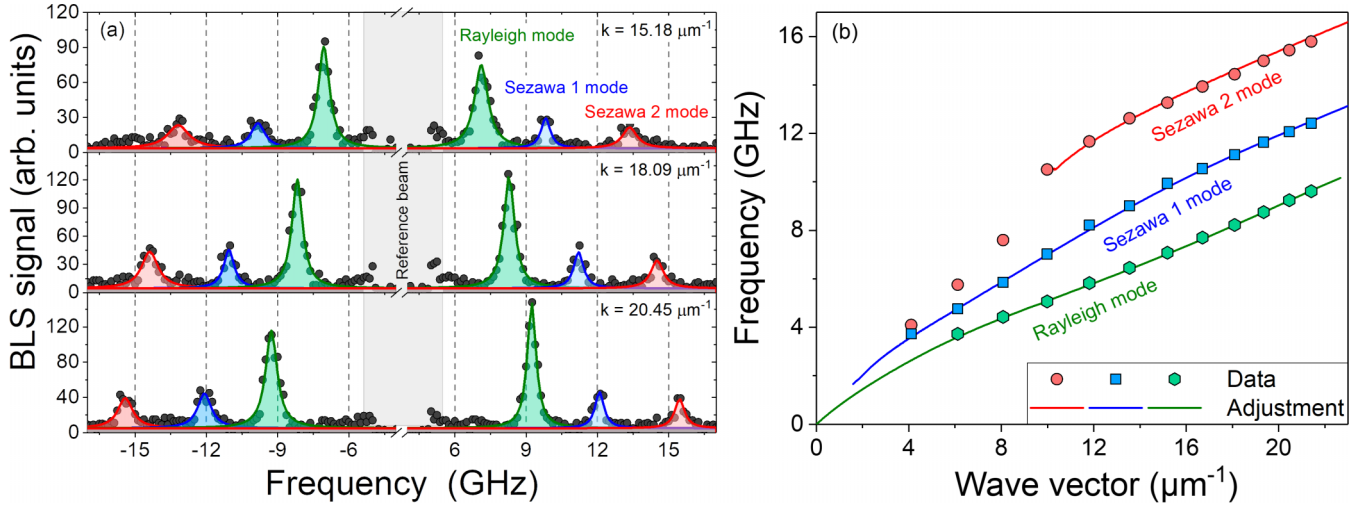

FIG. 2. Room-temperature ($T = 25\,^{\circ}$C), antiferromagnetic phase data: (a) BLS spectra at fixed temperature, variable wave vectors, and no applied external field. (b) Dispersion relationship of the first three acoustic surface modes: symbols refer to BLS data, and solid lines are calculations with the FeRh elastic coefficients $C_{11} = 219$, $C_{12} = 148$, and $C_{44} = 125$ GPa, optimized via the procedure described in the text.

variable wave-vector, giving access to dispersion relationships from which the elastic constants were extracted.

We first comment on the dispersion relationship measurements, performed upon warming, from $T = 25$ to $121\,^{\circ}$C. The measured frequencies reflect the effective acoustic velocities of the entire FeRh film over the MgO substrate system. Because acoustic waves in the magnetic film are *slower* than in the substrate, a dispersive character is obtained, as clearly evidenced in Fig. 2(b) (room-temperature measurement). Surface acoustic waves have an evanescent decay perpendicular to the surface with a depth of the order of the acoustic wavelength ($2\pi/k$). As the wave vector increases, the corresponding acoustic wavelength decreases, exploring a volume with a larger fraction of FeRh. At the lowest wave vector, it is essentially only the MgO substrate that is probed. For the largest probed wave vector, $k = 21.4\ \mu\text{m}^{-1}$, the corresponding phonon wavelength is $\lambda = 294$ nm, a little thicker than the film.

We now consider how the acoustic frequencies vary during a complete temperature warming/cooling cycle at fixed $k = 15.18\ \mu\text{m}^{-1}$ (Fig. 3). Strikingly, by comparing similar temperatures on the warming and cooling branches, one clearly observes a hysteresis opening up, e.g., about 0.63 GHz for the first Sezawa mode, 0.46 GHz for the second one, and 0.17 GHz for the Rayleigh mode. This behavior is due to the hysteretic nature of the first-order AF $\leftrightarrow$ FM phase transition of FeRh, which can be probed by the acoustic waves given the appreciable ratio λ/d between the wavelength and thickness. The onsets of the transition for the heating and cooling branches occur in the same temperature range as presented earlier (Fig. 1), about 5–7 °C lower than for the reflectivity data. This difference is well explained by the downshift of the transition temperature under magnetic field (the $-8\,^{\circ}$C/T shift recorded by Maat *et al.* [26] leads to a $-1.6\,^{\circ}$C shift for the 200 mT field applied here), and by the static heating induced by the CW laser beam, estimated using the thermal conductivity of FeRh to 7 °C at most [27]. Finally, we emphasize that, away from the transition on either side, all mode frequencies decrease with increasing temperature, a signature of the usual decrease of acoustic velocities upon warming.

V. PICOSECOND ACOUSTIC MEASUREMENT OF C_{11}

The temperature-dependent BLS measurements give a set of dispersion relations in the AF and FM phases. They reflect the values of the (unknown) FeRh and (known) MgO elastic constants, the (known) film thickness, and the material volume density. To narrow the parameter space to determine the C'_{ij}s, we measure the longitudinal (bulk) acoustic wave velocity independently.

For this, we use a standard pump-probe technique in which a pump beam impinging on the metallic FeRh surface generates a picosecond-long acoustic pulse [28]. The probe beam is

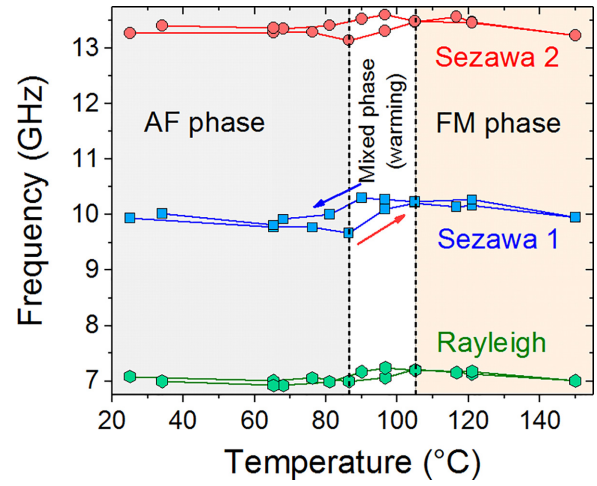

FIG. 3. Acoustic frequencies of the Rayleigh and first two Sezawa modes, measured at $k = 15.18\ \mu\text{m}^{-1}$ vs temperature. The background color illustrates the nature of the magnetic phase (uniform antiferromagnetic or ferromagnetic, and mixed for the warming branch).

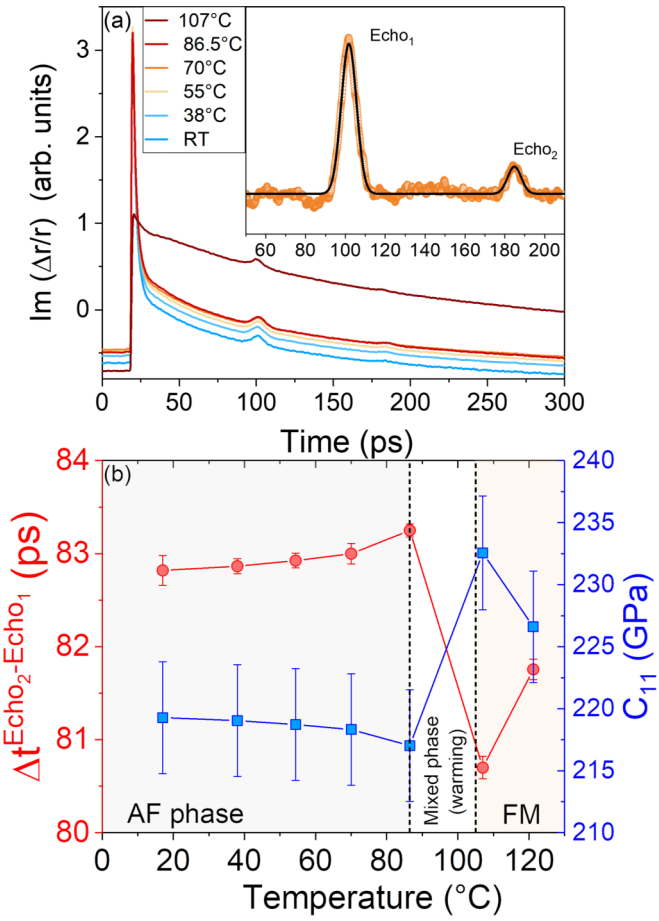

FIG. 4. (a) Longitudinal picosecond acoustic wave interferometry at different temperatures, in the AFM phase up to 86.5 °C, and in the FM phase above. Inset: the arrival times of the echoes are found by fitting the data after removal of the thermal background (here $T = 70\,^{\circ}\mathrm{C}$). See Appendix B for experimental details. (b) The difference in echo arrival time gives the velocity, and from there C_{11} knowing the volume density.

passed through a Sagnac interferometer in order to detect the displacement of the surface. Please refer to Appendix B for more experimental details on this technique.

A typical time delay scan [Fig. 4(a)] results in an electronic peak at the pump-probe coincidence, followed by a slow decay over which appear features (echoes), corresponding to the displacement of the surface upon arrival of the acoustic wave after reflection off the FeRh/MgO interface. We point out that the electronic response is much stronger in the AF phase. While a proper analysis of this interesting feature is beyond the scope of this paper, we suggest this might be attributed to the more electrically resistive nature of the low-temperature phase. Within our time window, two echoes are clearly visible, separated in time by a delay Δt related to the longitudinal velocity $\Delta t = \frac{2d}{V_L}$. Measurements are then performed at discrete rising temperature values on the warming branch of the transition, and the values of $\Delta t(T)$ and $V_L(T)$ are estimated precisely (see Appendix B for details). Using the temperature/phase dependence of the volume density (see Appendix C), we obtain the thermal variations of $C_{11}(T)$ using $V_L(T) = \sqrt{\frac{C_{11}(T)}{\rho(T)}}$ [Fig. 4(b)]. The main source of error comes from the ± 2 nm uncertainty on the $d = 195$ nm layer thickness.

As is often the case in solid crystals, C_{11} decreases steadily with temperature. It undergoes a steep jump upon crossing the transition (between $T = 86$ and $107\,^{\circ}\mathrm{C}$). Despite being minute (a mere 2 ps), the difference in echo delays at the onset of the transition ($T = 86\,^{\circ}\mathrm{C}$) undoubtedly points to a larger C_{11} constant in the FM phase, with $C_{11,\mathrm{AF}} \approx 216$–218 GPa between 25 and 86 °C, and $C_{11,\mathrm{FM}} \approx 228$–232 GPa ($T > 105\,^{\circ}\mathrm{C}$). These values align with those found by previous authors [12,13]: Cooke *et al.* had similarly found an increase of C_{11} from 218 to 236 GPa when going from AF to FM by changing the Rh concentration, at $T = 25\,^{\circ}\mathrm{C}$.

VI. DETERMINATION OF THE ELASTIC CONSTANTS

A. Fitting procedure

We now follow the "layer-on-substrate" approach of Farnell and Adler [29] to derive the frequency versus wave-vector $f(k)$ relationship of surface acoustic waves propagating along $x||[100]$ ([110]) in MgO (in FeRh). The elastic constants of both materials are expressed in the [100] reference frame of MgO, labeling C^*_{ij} the $\pi/4$-rotated C_{ij} elastic constants of FeRh, and $C_{0,ij}$ those of MgO (see Appendix C for the explicit expressions of the $[C]$, $[C^*]$, and $[C_0]$ tensors). Displacement waves in both materials are taken as linear combinations of z-damped terms of the general form $u_i = U_i e^{-\alpha z} e^{j(kx-\omega t)}$ with $i = x, z$, $\omega = 2\pi f = Vk$, and $j = \sqrt{-1}$. Injecting these in the elastic dynamical equation and imposing the adequate boundary conditions gives a system of six equations, whose determinant $\mathscr{D}(V)$ must be nullified:

$$\mathscr{D}(V) = \begin{vmatrix} 1 & 1 & -1 & -1 & -1 & -1 \\ r_{0,1} & r_{0,2} & -r_1 & -r_2 & -r_3 & -r_4 \\ a_{0,1} & a_{0,2} & -a_1 & -a_2 & -a_3 & -a_4 \\ b_{0,1} & b_{0,2} & -b_1 & -b_2 & -b_3 & -b_4 \\ 0 & 0 & a_1 e^{q_1 kh} & a_2 e^{q_2 kh} & a_3 e^{q_3 kh} & a_4 e^{q_4 kh} \\ 0 & 0 & b_1 e^{q_1 kh} & b_2 e^{q_2 kh} & b_3 e^{q_3 kh} & b_4 e^{q_4 kh} \end{vmatrix}. \tag{1}$$

The full procedure is described at length in Appendix C, as well as the explicit dependency of the coefficients r, a, and b on the elastic coefficients of FeRh and V. The roots V_i of Eq. (1) correspond to the different acoustic modes, the lowest one being the Rayleigh wave, and the second and third being the first and second Sezawa modes. It is then straightforward to compute $f_i(k) = \frac{V_i k}{2\pi}$ in order to compare with the experimental $f_{\mathrm{exp}}(k_{\mathrm{exp}})$ of Fig. 2(b).

Inspired by previous work [22,30], we find the elastic constants of FeRh by testing numerically a large set of (C_{11}, C_{12}, C_{44}) values. C_{11} is set by the picosecond acoustics measurements [Fig. 4(b)], while C_{12} was typically searched between 120 and 200 GPa, and C_{44} between 70 and 150 GPa in steps of 1 GPa. All the corresponding combinations were tested, and we choose the best solution as the triplet that minimizes

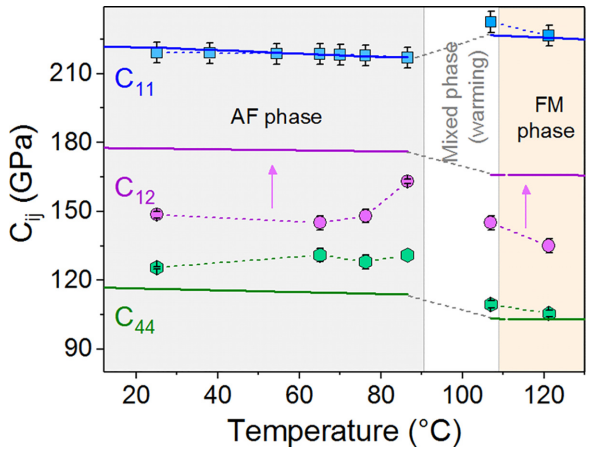

FIG. 5. Temperature-dependence of elastic constants of FeRh, determined by the analysis of the BLS and picosecond acoustics data (symbols with dashed lines, at more temperatures for the latter), or calculated by TDEP anharmonic lattice dynamics (full lines). Note that the latter were obtained in *both* phases in the entire temperature range, and that we are only showing values relevant to the experimentally observed phases.

the following figure of merit χ:

$$\chi = \sum_p \sum_l |\mathscr{D}(C_{11}, C_{12}, C_{44}, k_{\mathrm{exp},l}, V_p(k_{\mathrm{exp},l}))|^2. \quad (2)$$

In this expression, $p = 1, 2, 3$ labels the Rayleigh, first, and second Sezawa modes, $l = 1, \ldots, N_l$ are the data points for a given mode number, and $V_p(k_{\mathrm{exp},p}) = \frac{2\pi f_{\mathrm{exp},l,p}}{k_{\mathrm{exp},p}}$ is the velocity computed from the experimentally observed mode frequency at wave vector $k_{\mathrm{exp},p}$.

B. Results

A typical adjustment in the AF phase at room temperature is shown in Fig. 2(b), with the resulting calculated dispersion relation of the three acoustic modes plotted in full lines. An excellent agreement with the experimental data is found for the following FeRh constants: $C_{11} = 219$, $C_{12} = 148$, and $C_{44} = 125$ GPa. Note that the calculated Sezawa modes only exist above a particular cutoff wave vector ($k_{S1} = 1.58$ and $k_{S2} = 10.25\ \mu\mathrm{m}^{-1}$), a well-known feature of these semiguided surface modes [29]. The fact that we nevertheless observe the guided modes below k_{S2} might be due to a slight misalignment off high-symmetry crystalline axis. We have discarded these points from the fitting procedure and only used points in the interval $k = 13$–$21.4\ \mu\mathrm{m}^{-1}$. The fitting procedure is applied to all the temperatures of the warming branch of Fig. 3. The resulting temperature-dependent FeRh elastic constants are shown in Fig. 5, with the error bars reflecting the uncertainty on the film thickness ($d = 195 \pm 2$ nm).

We find C_{44} has a rather flat behavior with temperature in the AF phase, and then decreases from 130 to 110 GPa at the transition. This drop is similar to the one seen by Cooke *et al.*, albeit on very different values (77 to 57 GPa) estimated quite indirectly from a heat-capacity measurement. We evidence a nonmonotonic evolution of C_{12} in the AF phase, with a sharp increase (≈20 GPa) as the FM phase is approached. While this is not unheard of [C_{12}(T) of MgO is, for instance, nonmonotonous at low temperatures [31]], one might wonder whether it is related to the volume increase taking place at the transition. There is no previous record of any estimate of C_{12} in either phase with which to compare our results. Instead, we can "isotropize" our coefficients into a Young modulus E, using the well-known Hill method [32], and compare it to values of the literature. We find in the AF phase $E_{\mathrm{AF}} = 187$ GPa ($T = 86\,^\circ$C), and a higher value $E_{\mathrm{FM}} = 198$ GPa in the FM phase ($T = 107\,^\circ$C). This is reassuringly similar to the values found on polycrystalline FeRh by both Palmer *et al.* [13]: $E_{\mathrm{AF}} = 196$ and $E_{\mathrm{FM}} = 211$ GPa ($T \approx 40\,^\circ$C), and by Ricodeau *et al.* [14,33]: $E_{\mathrm{AF}} = 170$ ($T \approx 25\,^\circ$C) and $E_{\mathrm{FM}} = 190$ GPa ($T \approx 100\,^\circ$C). Let us recommend comparing absolute values of the elastic coefficients in different phases with caution if taken at very different temperatures, or Rh concentration, since both of these parameters have a strong influence. Comparing to other materials, it is worth mentioning that the elastic constants of FeRh (i) vary overall more weakly with temperature than for instance those of Fe [34] or MgO [31] (for which C_{11} loses ≈6 GPa, C_{12} ≈0.5 GPa, and $C_{44} \approx 1$–2 GPa between 25 and 125 °C), and (ii) are very similar, in the FM phase, to those of crystalline iron taken at a similar temperature ($T = 125\,^\circ$C [34]): $C_{11} = 225$, $C_{12} = 133$, $C_{44} = 114$ GPa, to be compared to those we found for FeRh in the FM phase: $C_{11} = 227$, $C_{12} = 135$, $C_{44} = 105$ GPa.

VII. NUMERICAL ESTIMATES OF C_{ij} OF FeRh

We now discuss the first-principles modeling of the elastic constants of FeRh. To compare quantitatively to our experiments, it is essential to go beyond the harmonic approximation by including thermal expansion and intrinsic anharmonicity, in particular for AF FeRh. Existing $T = 0$ K theoretical studies in the literature predict the appearance of an imaginary phonon mode [17,35–37], which prevents the evaluation of thermodynamic quantities.

We employ the temperature-dependent effective potential (TDEP) method [38–40] to include anharmonicity and renormalize phonon-phonon interactions. To reduce the simulation costs while keeping the accuracy of DFT, we constructed two machine-learning interatomic potential (MLIP [41]) models for the FM and AF phases. The details of the simulations are described in Appendix D. We calculate the elastic constants of both phases as a function of T (0–500 K, i.e., −273 to 227 °C) through their relation to the real-space interatomic force constants. Aschauer *et al.* [17] in particular showed the importance of nonlinear elasticity in FeRh. These effects on the measured C_{ij} are folded in through the temperature dependence of the TDEP force constants.

Considering first $T = 0$ K DFT values, Table I shows that our results compare well with available literature [16,17,19], with slight differences that can be attributed to the choice of exchange and correlation functionals or the use of DFT + U. The temperature dependence of the elastic constants of FeRh in both phases are then shown in Fig. 5, with values cut off to mimic the experimentally observed warming transition.

When comparing with the experimentally determined values of C_{11}, C_{12}, and C_{44}, a particularly good agreement is obtained for C_{11} in both phases, with a maximum discrepancy

TABLE I. Survey of the elastic constants of the C_{ij} constants of FeRh obtained by DFT computations and this work, at 25 °C in the AF phase and 121 °C in the FM phase, and comparison to our experimental data.

Phase		C_{11} (GPa)	C_{12} (GPa)	C_{44} (GPa)
	This work exp 25 °C	219	148	125
	This work DFT 25 °C	224	177	116
AF	This work DFT 0 K	239	184	129
	He *et al.* DFT 0 K [16]	219	188	120
	Aschauer *et al.* DFT 0 K [17]	225	181	120
	This work exp 121 °C	227	135	105
	This work DFT 121 °C	225	165	103
FM	This work DFT 0 K	262	169	111
	He *et al.* DFT 0 K [16]	278	179	110
	Aschauer *et al.* DFT 0 K [17]	252	161	110
	Hao *et al.* DFT 0 K [19]	259	162	111

(in absolute value) of 2.4%. For the other C'_{ij}s, the agreement is good overall, with a maximum discrepancy (in absolute value) of 23% for C_{12} and 13% for C_{44}. More importantly, the temperature evolution is well described, particularly the changes when going from the AF to the FM phase. It should be noted that explicitly including atomic vibrations in the temperature evolution is important for a quantitative description. In particular, and as shown in Appendix D, only including thermal expansion as a mechanism for the temperature evolution results in an overestimation of the C_{11} in the FM phase and the C_{44} in the AF phase.

VIII. CONCLUSIONS

We measured the phonon dispersion relationship of epitaxial FeRh/MgO using Brillouin light scattering at variable temperature in both the uniform ferro- and antiferromagnetic phases of this material. Modeling the obtained dispersion by a "layer-on-substrate" approach, using the known parameters of MgO, and the independently measured C_{11} constant, we obtained the other two constants; C_{12}(T) and C_{44}(T). As is very often the case, C_{11} is substantially larger than the other two. Unlike the latter two, C_{11} is larger in the FM phase than in the AF phase. A temperature-dependent first-principles modeling of the elastic constants renders the experimental values very closely. This work represents a substantial step towards the accurate modeling of the magnon-phonon interaction, thanks to a proper description of the elastic system in both phases, and at varying temperature. In this respect, it should also provide a new tool to determine the role of strain in the intriguing first-order AF-FM transition of FeRh.

ACKNOWLEDGMENTS

This work has been partly supported by the French Agence Nationale de la Recherche (ANR ACAF 20-CE30-0027). Access to the CEITEC Nano Research Infrastructure was supported by the Ministry of Education, Youth and Sports (MEYS) of the Czech Republic under the project Czech-NanoLab (LM2023051). A.C. and M.J.V. acknowledge the Fonds de la Recherche Scientifique (FRS-FNRS Belgium) for PdR Grant No. T.0103.19 - ALPS, and ARC project DREAMS (G.A. 21/25-11) funded by Fédération Wallonie Bruxelles and ULiege. Simulation time was awarded by the Belgian share of EuroHPC in LUMI hosted by CSC in Finland, by the CECI (FRS-FNRS Belgium Grant No. 2.5020.11), as well as the Zenobe Tier-1 of the Fédération Wallonie-Bruxelles (Walloon Region Grant Agreement No. 1117545). We acknowledge the technical assistance of Mathieu Bernard from Institut des Nanosciences de Paris.

APPENDIX A: DETAILS ON THE HEATING SYSTEM INTEGRATED IN THE BLS SETUP

To study the sample in both AF and FM phases, an *in situ* heating system was integrated into the BLS bench. This system is placed in the air gap of an electromagnet consisting of a cylindrical oven with an internal diameter of 1 Cm, having an electrical resistance of 380 Ω powered by a dc current source to ensure the heating. The sample is held on a metal rod with a thermal paste, inserted into the oven near a thermocouple probe to get the heating temperature, which is adjusted from ambient to 150 °C corresponding to a maximum current of 260 mA. For each temperature, the heating process, thermal equilibrium, and spectrum acquisition take around 3 h, corresponding on average to 1 count/min for the Rayleigh peak.

APPENDIX B: PICOSECOND ACOUSTICS

The picosecond acoustics pump-probe setup is described in Ref. [28]. The Sagnac interferometer measures $\mathrm{Im}(\Delta r/r)$, where r is the amplitude reflection coefficient of the light electric field. One can show that this quantity gives the modification of the phase of the electric field of the light induced by the vertical displacement of the sample surface [42]. More specifically to these measurements, the laser repetition rate was 80 MHz, with a modulation of the pump at 1 MHz. Its wavelength was 773 nm, and the beam diameter was of the order of ≈15 μm. The power of the pump beam was around $P = 32$ mW, and that of the probe was around 4 mW. The delay line was scanned mechanically at 40 nm/ps. To determine precisely the arrival time of the echoes, the thermal background is removed, and the peaks are fitted by a Lorentzian [inset of Fig. 4(a)].

APPENDIX C: DETAILS ON THE MODELING OF THE ACOUSTIC DISPERSION

In this Appendix, we give the cumbersome details on how the determinant of Eq. (1) is obtained. It is then used to determine the elastic constants of FeRh from the dispersion relation measured by BLS.

Waves and tensors are all given in the ⟨100⟩ reference frame of the cubic MgO substrate. For MgO, we have

$$[C_0] = \begin{pmatrix} C_{0,11} & C_{0,12} & C_{0,12} & 0 & 0 & 0 \\ C_{0,12} & C_{0,11} & C_{0,12} & 0 & 0 & 0 \\ C_{0,12} & C_{0,12} & C_{0,11} & 0 & 0 & 0 \\ 0 & 0 & 0 & C_{0,44} & 0 & 0 \\ 0 & 0 & 0 & 0 & C_{0,44} & 0 \\ 0 & 0 & 0 & 0 & 0 & C_{0,44} \end{pmatrix}.$$

The elastic coefficient tensor of cubic FeRh has an identical symmetry, but needs to be rotated $\pi/4$ to render the epitaxial match condition of the layer on its substrate:

$$[C^*] = \begin{pmatrix} C^*_{11} & C^*_{12} & C^*_{13} & 0 & 0 & 0 \\ C^*_{12} & C^*_{11} & C^*_{12} & 0 & 0 & 0 \\ C^*_{13} & C^*_{12} & C^*_{33} & 0 & 0 & 0 \\ 0 & 0 & 0 & C^*_{44} & 0 & 0 \\ 0 & 0 & 0 & 0 & C^*_{44} & 0 \\ 0 & 0 & 0 & 0 & 0 & C^*_{66} \end{pmatrix}$$

with

$$\begin{aligned} C^*_{11} &= \tfrac{1}{2}(C_{11} + C_{12}) + C_{44}, \\ C^*_{12} &= \tfrac{1}{2}(C_{11} + C_{12}) - C_{44}, \\ C^*_{13} &= C_{12}, \\ C^*_{33} &= C_{11}, \\ C^*_{44} &= C_{44}, \\ C^*_{66} &= \tfrac{1}{2}(C_{11} - C_{12}). \end{aligned}$$

Following Farnell *et al.* [29], the procedure to obtain the dispersion relationship of the FeRh/MgO system is the following: (i) fix a wave vector k, (ii) calculate the implicit relationship relating the Rayleigh wave velocity V to the elastic constants of each material, and (iii) find the solution $V(k)$ satisfying the boundary conditions at the film/substrate and air/film interfaces.

With z the normal to the film and $x||[100]$, the partial waves propagating in MgO and FeRh along x are, respectively, of the form

$$u_0(x,z,t) = \sum_{i=1,2} \begin{pmatrix} U_{x,0i} \\ 0 \\ U_{z,0i} \end{pmatrix} e^{-q_{0,i}kz} e^{j(\omega t - kx)}, \tag{C1}$$

$$u(x,z,t) = \sum_{i=1-4} \begin{pmatrix} U_{x,i} \\ 0 \\ U_{z,i} \end{pmatrix} e^{-q_i kz} e^{j(\omega t - kx)}. \tag{C2}$$

The dimensionless coefficients $q_{0,i}, q_i$ convey the penetration profile of the displacements u, u_0. Injecting these wave-forms into the elastic equation of motion leads to the two quadratic equations (C3) and (C4). We label $q_{i,0}$ $(i = 1, 2)$ the two roots of Eq. (C3) exhibiting a positive real part, and q_i $(i = 1\text{–}4)$ the four roots of Eq. (C4). ρ_0 and ρ are the volume densities of MgO and FeRh, respectively,

$$q_0^4 + \left(\frac{-C_{0,44}^2 - C_{0,11}^2 + (C_{0,12} + C_{0,44})^2 + \rho_0 V^2 (C_{0,11} + C_{0,44})}{C_{0,11} C_{0,44}} \right) q_0^2 + \frac{(\rho_0 V^2 - C_{0,11})(\rho_0 V^2 - C_{0,44})}{C_{0,11} C_{0,44}} = 0, \tag{C3}$$

$$q^4 + \left(\frac{-C_{44}^{*2} - C_{11}^* C_{33}^* + (C_{13}^* + C_{44}^*)^2 + \rho V^2 (C_{33}^* + C_{44}^*)}{C_{33}^* C_{44}^*} \right) q^2 + \frac{(\rho V^2 - C_{11}^*)(\rho V^2 - C_{44}^*)}{C_{33}^* C_{44}^*} = 0. \tag{C4}$$

The ratios of the amplitudes of the out-of-plane and in-plane displacements for each solution in MgO and FeRh are labeled $r_{0,i}$ and r_i. They are given by Eqs. (C5) and (C6), in which we recall that the $q_{0,i}$, q_i depend on V,

$$r_{0,i}(V,k) = \frac{U_{z,0i}}{U_{x,0i}} = \frac{C_{11,0} - q_{0,i}^2 C_{44,0} - \rho_0 V^2}{j q_{0,i} (C_{12,0} + C_{44,0})}, \tag{C5}$$

$$r_i(V,k) = \frac{U_{z,i}}{U_{x,i}} = \frac{C_{11}^* - q_i^2 C_{44}^* - \rho V^2}{j q_i (C_{13}^* + C_{44}^*)}. \tag{C6}$$

Finally, the conditions of continuous displacements and tangential and normal stresses across the interface, and zero stress at the surface, lead to a system of six equations with six unknown amplitudes $(U_{x,01}, U_{x,02}, U_{x,1}, U_{x,2}, U_{x,3}, U_{x,4})$. To find the velocity V corresponding to the chosen k, one must thus find the roots V_i of the 6×6 determinant $\mathscr{D}(V)$ given in the main text, Eq. (1). The velocity intervenes through the dependency $q_{0,i}(V,k)$, $q_i(V,k)$ and $r_{0,i}(V,k)$, $r_i(V,k)$ in the coefficients $a_{0,i}$, a_i and $b_{0,i}$, b_i:

$$a_{0,i}(V,k) = \frac{C_{44,0}}{C_{44}} (q_{0,i} + j r_{0,i}), \tag{C7}$$

$$a_i(V,k) = q_i + j r_i, \tag{C8}$$

$$b_{0,i}(V,k) = j C_{12,0} + C_{11,0} q_{0,i} r_{0,i}, \tag{C9}$$

$$b_i(V,k) = j C_{13}^* + C_{33}^* q_i r_i. \tag{C10}$$

The numerical values for $C_{0,ij}(T)$ and $\rho_0(T)$ of MgO were taken from Sumino *et al.* [31]. The volume density of FeRh was taken phase-dependent with $\rho_{\mathrm{FM}} = \rho_{\mathrm{AF}}/1.007 = 9820$ kg m^{-3}, where $\rho_{\mathrm{AF}} = 9888.49$ kg m^{-3} was computed from in-plane and out-of-plane lattice parameters $a_{||,\mathrm{AF}} = 2.987$ Å and $c_{\perp,\mathrm{AF}} = 2.988$ Å measured by x-ray diffraction at room temperature [9,24].

APPENDIX D: DETAILS ON THE FIRST-PRINCIPLES ANHARMONIC MODELING

1. First-principles forces and machine-learning interatomic potential

As a reference potential for the MLIP, we performed DFT calculations with the ABINIT suite [43,44] using the PBE [45] parametrization of the exchange and correlation functional in the PAW formalism [46,47]. To ensure the convergence of the calculations, the kinetic energy cutoff was set to 20 Ha, while the Brillouin zone integration was discretized on a $21 \times 21 \times 21$ k-point grid. The ground-state lattice constants obtained with these parameters are shown in Table II. They are in agreement with previous theoretical results [17,37] and very close to room-temperature experimental values [24].

The MLIP were constructed using the moment tensor potential [41,48]. For both phases, we set the level of the MLIP to 22, and a cutoff of 5.6 Å is used, in order to

TABLE II. Comparison of structural properties at 0 K computed with DFT and the MLIP using finite deformation and fitted using the elastic package [52].

	a (Å)	C_{11} (GPa)	C_{12} (GPa)	C_{44} (GPa)
DFT AF	3.004	231	188	121
MLIP AF	3.004	239	184	129
DFT FM	3.019	267	169	114
MLIP FM	3.020	262	169	111

ensure an accurate description of important interactions for the B2 structure [49]. In the AF phase, to account for the spin-dependent interactions between atoms, the spin-up and -down Fe atoms were considered as distinct elements in the descriptor. The DFT data set was constructed self-consistently following the MLACS algorithm [50], in which a molecular-dynamics trajectory is driven by a MLIP which is trained regularly on configurations extracted from this dynamics. It should be noted that the configurations are chosen randomly and not based on an extrapolation criterion [51] to improve on the measure defined in [50]. After each new addition to the database, the thermostat and barostat of the MD run were set to randomly generated temperature and pressure in the range 20–1200 K and −2 to 2 GPa, to ensure a stable MLIP in the range of thermodynamic conditions considered in this work. To improve the description of elastic properties, some strained configurations were also included in the data set. Once enough data are available, the potential is validated by splitting the data set into testing and training sets, and the final MLIP were fit using the energy, forces, and stress.

The resulting MLIP provides an accurate representation of the potential energy surface provided by the DFT, as shown in the good agreement for structural properties in Table II, and the energy, forces, and stress correlation shown in Fig. 6.

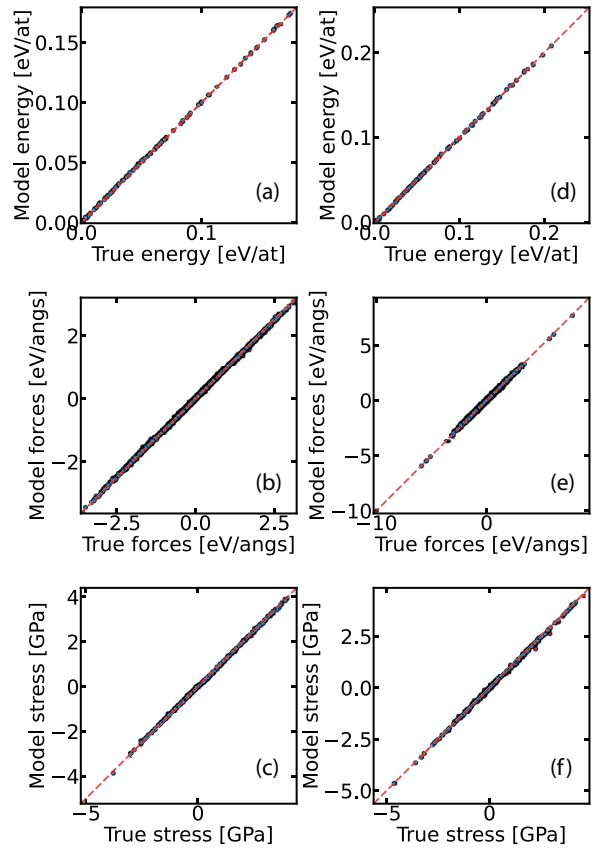

FIG. 6. Correlation plot between the MLIP and the DFT data sets. Plots (a), (b), and (c) are for the AF phase, and (d), (e), and (f) are for the FM phase.

2. Molecular dynamics

With the MLIP, we compute the effective anharmonic Hamiltonian from 50 to 450 K in steps of 50 K. For each temperature, we run two 100 ps MD simulations on $8 \times 8 \times 8$ supercells, with a time step of 1 fs using the LAMMPS package [53]. The first MD run is performed in the NPT (isothermal-isobaric) ensemble, and is used to compute the average equilibrium volume, while the second one employs this equilibrium volume in the NVT (canonical) ensemble. Postprocessing is done using 900 uncorrelated configurations, extracted from the MD trajectory after 25 ps of equilibration.

3. Temperature-dependent elastic constants

To describe the influence of the temperature on the elastic constants, a common approximation is to neglect the explicit effects of atomic vibrations and consider that the C_{ij} evolve only through the thermal expansion as

$$C_{\alpha\beta\gamma\delta}(\Omega, T) = C_{\alpha\beta\gamma\delta}(\Omega(T), 0), \tag{D1}$$

where $\Omega(T)$ is the volume. While this method often brings a good description of the temperature evolution of the elastic constants, it is important to account for the explicit effects of the temperature to be quantitative.

To go beyond this approximation, we can use the fact that elastic constants are related to long-wavelength phonons and can be extracted using the slope of the acoustic dispersion close to the Γ point. Then, introducing the temperature evolution of the phonons to extract the slope allows us to include the effects of temperature on the elastic properties. The slope

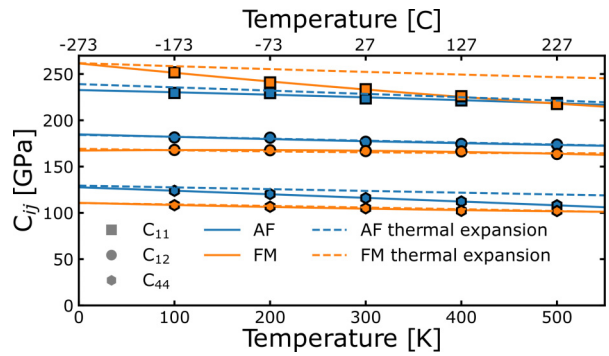

FIG. 7. Theoretical prediction of C'_{ij}s of FeRh in the FM and AF phases. Markers are the direct prediction of the elastic constants using the TDEP method, and full lines are a third-order polynomial fit. Dashed lines present results when only considering thermal expansion in the temperature evolution of the elastic constants.

of the acoustic dispersion can be directly extracted from the interatomic force constants $\mathbf{\Phi}$ as [54,55]

$$C_{\alpha\beta\gamma\delta}(\Omega, T) = -\frac{1}{2\Omega}\sum_{ij}\Phi_{ij}^{\alpha\beta}(\Omega, T)d_{ij}^{\gamma}d_{ij}^{\delta}, \tag{D2}$$

where d_{ij}^{γ} is the distance between the unit cells of atoms i and j along the Cartesian direction γ.

To introduce finite-temperature renormalization of the interatomic force constant, and consequently of the $C_{\alpha\beta\gamma\delta}$ tensor, we use the temperature-dependent effective potential (TDEP) method. The method works by performing a least-squares fit of the $\mathbf{\Phi}(\Omega, T)$ tensor using a set of forces and displacements extracted from an NVT molecular dynamics run [38,39]. We used the implementation provided by the TDEP package [56].

We compare the temperature dependence of both approaches in Fig. 7. While most of the C_{ij} changed very little when introducing atomic vibrations in the description, the FM C_{11} and the AF C_{44} are significantly reduced.

[1] M. Fallot, Les alliages du fer avec les métaux de la famille du platine, Ann. Phys. **11**, 291 (1938).

[2] T. Moriyama, N. Matsuzaki, K.-J. Kim, I. Suzuki, T. Taniyama, and T. Ono, Sequential write-read operations in FeRh antiferromagnetic memory, Appl. Phys. Lett. **107**, 122403 (2015).

[3] X. Marti, I. Fina, C. Frontera, J. Liu, P. Wadley, Q. He, R. J. Paull, J. D. Clarkson, J. Kudrnovský, I. Turek, J. Kuneš, D. Yi, J.-H. Chu, C. T. Nelson, L. You, E. Arenholz, S. Salahuddin, J. Fontcuberta, T. Jungwirth, and R. Ramesh, Room-temperature antiferromagnetic memory resistor, Nat. Mater. **13**, 367 (2014).

[4] H. Wu, H. Zhang, B. Wang, F. Groß, C. Y. Yang, G. Li, C. Guo, H. He, K. Wong, D. Wu, X. Han, C. H. Lai, J. Gräfe, R. Cheng, and K. L. Wang, Current-induced Néel order switching facilitated by magnetic phase transition, Nat. Commun. **13**, 1 (2022).

[5] N. A. Blumenschein, G. M. Stephen, C. D. Cress, S. W. LaGasse, A. T. Hanbicki, S. P. Bennett, and A. L. Friedman, High-speed metamagnetic switching of FeRh through Joule heating, Sci. Rep. **12**, 22061 (2022).

[6] Y. Liu, L. C. Phillips, R. Mattana, M. Bibes, A. Barthélémy, and B. Dkhil, Large reversible caloric effect in FeRh thin films via a dual-stimulus multicaloric cycle, Nat. Commun. **7**, 11614 (2016).

[7] J. Lyubina, Magnetocaloric materials for energy efficient cooling, J. Phys. D **50**, 053002 (2017).

[8] V. Uhlíř, J. A. Arregi, and E. E. Fullerton, Colossal magnetic phase transition asymmetry in mesoscale FeRh stripes, Nat. Commun. **7**, 13113 (2016).

[9] J. A. Arregi, O. Caha, and V. Uhlíř, Evolution of strain across the magnetostructural phase transition in epitaxial FeRh films on different substrates, Phys. Rev. B **101**, 174413 (2020).

[10] F. Pressacco, D. Sangalli, V. Uhlí, D. Kutnyakhov, J. A. Arregi, S. Y. Agustsson, G. Brenner, H. Redlin, M. Heber, D. Vasilyev, J. Demsar, G. Schönhense, M. Gatti, A. Marini, W. Wurth, and F. Sirotti, Subpicosecond metamagnetic phase transition in FeRh driven by non-equilibrium electron dynamics, Nat. Commun. **12**, 5088 (2021).

[11] S. O. Mariager, F. Pressacco, G. Ingold, A. Caviezel, E. Möhr-Vorobeva, P. Beaud, S. L. Johnson, C. J. Milne, E. Mancini, S. Moyerman, E. E. Fullerton, R. Feidenhans'l, C. H. Back, and C. Quitmann, Structural and magnetic dynamics of a laser induced phase transition in FeRh, Phys. Rev. Lett. **108**, 087201 (2012).

[12] D. W. Cooke, F. Hellman, C. Baldasseroni, C. Bordel, S. Moyerman, and E. E. Fullerton, Thermodynamic measurements of Fe-Rh alloys, Phys. Rev. Lett. **109**, 255901 (2012).

[13] S. B. Palmer, P. Dentschuk, and D. Melville, Elastic properties of an iron-rhodium alloy, Phys. Status Solidi A **32**, 503 (1975).

[14] J. A. Ricodeau and D. Melville, Model of the antiferromagnetic-ferromagnetic transition in FeRh alloys, J. Phys. F **2**, 337 (1972).

[15] A. Castets, D. Tochetti, and B. Hennion, Spin wave spectrum of iron-rhodium alloy in antiferromagnetic and ferromagnetic phases, Physica B+C **86-88**, 353 (1977).

[16] W. He, H. Huang, and X. Ma, First-principles calculations on elastic and entropy properties in FeRh alloys, Mater. Lett. **195**, 156 (2017).

[17] U. Aschauer, R. Braddell, S. A. Brechbühl, P. M. Derlet, and N. A. Spaldin, Strain-induced structural instability in FeRh, Phys. Rev. B **94**, 014109 (2016).

[18] M. J. Jiménez, A. B. Schvval, and G. F. Cabeza, *Ab initio* study of FeRh alloy properties, Comput. Mater. Sci. **172**, 109385 (2020).

[19] Y. Hao, L. Zhang, and J. Zhu, The electronic structure, phase transition, elastic, thermodynamic, and thermoelectric properties of FeRh: High-temperature and high-pressure study, Z. Naturforsch. A **75**, 789 (2020).

[20] J. Gump, H. Xia, M. Chirita, R. Sooryakumar, M. A. Tomaz, and G. R. Harp, Elastic constants of face-centered-cubic cobalt, J. Appl. Phys. **86**, 6005 (1999).

[21] G. Carlotti, J. Sadhu, and F. Dumont, Dependence of the different elastic constants of ScAlN films on Sc content: A Brillouin scattering study with polarization analysis, in *2017 IEEE International Ultrasonics Symposium (IUS)* (IEEE, Piscataway, NJ, 2017), pp. 1–5.

[22] J. O. Kim, J. D. Achenbach, P. B. Mirkarimi, M. Shinn, and S. A. Barnett, Elastic constants of single-crystal transition-metal nitride films measured by line-focus acoustic microscopy, J. Appl. Phys. **72**, 1805 (1992).

[23] P. Hemme, P. Djemia, P. Rovillain, Y. Gallais, A. Sacuto, A. Forget, D. Colson, E. Charron, B. Perrin, L. Belliard, and M. Cazayous, Elastic properties assessment in the multiferroic $BiFeO_3$ by pump and probe method, Appl. Phys. Lett. **118**, 062902 (2021).

[24] J. A. Arregi, F. Ringe, J. Hajduček, O. Gomonay, T. Molnár, J. Jaskowiec, and V. Uhlí, Magnetic-field-controlled growth of magnetoelastic phase domains in FeRh, J. Phys.: Mater. **6**, 034003 (2023).

[25] S. M. Rezende, A. Azevedo, and R. L. Rodríguez-Suárez, Introduction to antiferromagnetic magnons, J. Appl. Phys. **126**, 151101 (2019).

[26] S. Maat, J.-U. Thiele, and E. E. Fullerton, Temperature and field hysteresis of the antiferromagnetic-to-ferromagnetic phase transition in epitaxial FeRh films, Phys. Rev. B **72**, 214432 (2005).

[27] The maximum temperature rise in Fig. 3 ($k = 15.18\mu m^{-1}$, incident angle of 40°) was estimated using a layer-on-substrate approach and thermal conductivities κ_{th} of FeRh and MgO of Ref. [57]; in particular, $\kappa_{th} = 30$ (10) W m^{-1} K^{-1} in the AF (FM) phase. The effective incident power was taken as $(1 - R)P_{inc}$ with $R = 0.55$ in the FM phase (smaller than $R = 0.66$ in the AF phase) at $\lambda_{BLS} = 532$ nm [57], and a beam radius of 60 μm.

[28] E. Péronne, N. Chuecos, L. Thevenard, and B. Perrin, Acoustic solitons: A robust tool to investigate the generation and detection of ultrafast acoustic waves, Phys. Rev. B **95**, 064306 (2017).

[29] W. G. W. Farnell, Types and properties of surface, in *Acoustic Surface Waves*, Topics in Applied Physics (Springer, Berlin, 1978), pp. 13–60.

[30] M. R. Karim and A. K. Mal, Inversion of leaky Lamb wave data by simplex algorithm, J. Acoust. Soc. Am. **88**, 482 (1990).

[31] Y. Sumino, O. L. Anderson, and I. Suzuki, Temperature coefficients of elastic constants of single crystal MgO between 80 and 1,300 K, Phys. Chem. Miner. **9**, 38 (1983).

[32] R. Hill, The elastic behaviour of a crystalline aggregate, Proc. Phys. Soc. London, Sect. A **65**, 349 (1952).

[33] A. I. Zakharov, A. M. Kadomtseva, R. Z. Levitin, and E. G. Ponyatovskil, Magnetic and magnetoelastic properties of a metamagnetic iron-rhodium alloy, Sov. Phys. JETP **19**, 1348 (1964).

[34] J. J. Adams, D. S. Agosta, R. G. Leisure, and H. Ledbetter, Elastic constants of monocrystal iron from 3 to 500 K, J. Appl. Phys. **100**, 113530 (2006).

[35] J. Kim, R. Ramesh, and N. Kioussis, Revealing the hidden structural phases of FeRh, Phys. Rev. B **94**, 180407(R) (2016).

[36] N. A. Zarkevich and D. D. Johnson, FeRh ground state and martensitic transformation, Phys. Rev. B **97**, 014202 (2018).

[37] M. P. Belov, A. B. Syzdykova, and I. A. Abrikosov, Temperature-dependent lattice dynamics of antiferromagnetic and ferromagnetic phases of FeRh, Phys. Rev. B **101**, 134303 (2020).

[38] O. Hellman, I. A. Abrikosov, and S. I. Simak, Lattice dynamics of anharmonic solids from first principles, Phys. Rev. B **84**, 180301(R) (2011).

[39] O. Hellman and I. A. Abrikosov, Temperature-dependent effective third-order interatomic force constants from first principles, Phys. Rev. B **88**, 144301 (2013).

[40] O. Hellman and D. A. Broido, Phonon thermal transport in Bi_2Te_3 from first principles, Phys. Rev. B **90**, 134309 (2014).

[41] A. V. Shapeev, Moment tensor potentials: A class of systematically improvable interatomic potentials, Multiscale Model. Simul. **14**, 1153 (2016).

[42] C. Thomsen, H. T. Grahn, H. J. Maris, and J. Tauc, Surface generation and detection of phonons by picosecond light pulses, Phys. Rev. B **34**, 4129 (1986).

[43] X. Gonze, B. Amadon, G. Antonius, F. Arnardi, L. Baguet, J.-M. Beuken, J. Bieder, F. Bottin, J. Bouchet, E. Bousquet, N. Brouwer, F. Bruneval, G. Brunin, T. Cavignac, J.-B. Charraud, W. Chen, M. Côté, S. Cottenier, J. Denier, G. Geneste *et al.*, The ABINITproject: Impact, environment and recent developments, Comput. Phys. Commun. **248**, 107042 (2020).

[44] A. H. Romero, D. C. Allan, B. Amadon, G. Antonius, T. Applencourt, L. Baguet, J. Bieder, F. Bottin, J. Bouchet, E. Bousquet, F. Bruneval, G. Brunin, D. Caliste, M. Côté, J. Denier, C. Dreyer, P. Ghosez, M. Giantomassi, Y. Gillet, O. Gingras *et al.*, ABINIT: Overview and focus on selected capabilities, J. Chem. Phys. **152**, 124102 (2020).

[45] J. P. Perdew, K. Burke, and M. Ernzerhof, Generalized gradient approximation made simple, Phys. Rev. Lett. **77**, 3865 (1996).

[46] P. E. Blöchl, Projector augmented-wave method, Phys. Rev. B **50**, 17953 (1994).

[47] F. Jollet, M. Torrent, and N. Holzwarth, Generation of projector augmented-wave atomic data: A 71 element validated table in the XML format, Comput. Phys. Commun. **185**, 1246 (2014).

[48] I. S. Novikov, K. Gubaev, E. V. Podryabinkin, and A. V. Shapeev, The MLIP package: Moment tensor potentials with MPI and active learning, Machine Learn.: Sci. Technol. **2**, 025002 (2021).

[49] S. Ono and D. Kobayashi, Role of the *M* point phonons for the dynamical stability of B2 compounds, Sci. Rep. **12**, 7258 (2022).

[50] A. Castellano, F. Bottin, J. Bouchet, A. Levitt, and G. Stoltz, *Ab initio* canonical sampling based on variational inference, Phys. Rev. B **106**, L161110 (2022).

[51] E. V. Podryabinkin and A. V. Shapeev, Active learning of linearly parametrized interatomic potentials, Comput. Mater. Sci. **140**, 171 (2017).

[52] P. T. Jochym and C. Badger, jochym/elastic: Maintenance release, Zenodo (2018), doi:10.5281/zenodo.593721.

[53] A. P. Thompson, H. M. Aktulga, R. Berger, D. S. Bolintineanu, W. M. Brown, P. S. Crozier, P. J. in 't Veld, A. Kohlmeyer, S. G. Moore, T. D. Nguyen, R. Shan, M. J. Stevens, J. Tranchida, C. Trott, and S. J. Plimpton, LAMMPS - a flexible simulation tool for particle-based materials modeling at the atomic, meso, and continuum scales, Comput. Phys. Commun. **271**, 108171 (2022).

[54] D. C. Wallace, *Statistical Physics of Crystals and Liquids* (World Scientific, Singapore, 2003), pp. 115–153.

[55] G. Leibfried and W. Ludwig, Theory of anharmonic effects in crystals, in *Solid State Physics* (Elsevier, Amsterdam, 1961), pp. 275–444.

[56] F. Knoop, N. Shulumba, A. Castellano, J. P. A. Batista, R. Farris, M. J. Verstraete, M. Heine, D. Broido, D. S. Kim, J. Klarbring, I. A. Abrikosov, S. I. Simak, and O. Hellman, TDEP: Temperature dependent effective potentials, J. Open Source Softw. **9**, 6150 (2024).

[57] A. Castellano, J. A. Arregi, V. Uhlí, B. Perrin, S. Université, and N. D. Paris, Magnetic phase dependency of the thermal conductivity of FeRh from thermoreflectance experiments and numerical simulations, HAL 1 (2024).